APPLIED SCIENCES AND ENGINEERING

Biomimetic human small muscular pulmonary arteries

Qianru Jin[1,2]*, Anil Bhatta[1,2]*, Jayson V. Pagaduan[1,2]*, Xing Chen[1,2]*, Hoku West-Foyle[3,6], Jiayu Liu[4], Annie Hou[2,5], Dan Berkowitz[1,5], Scot C. Kuo[3,5,6], Frederic B. Askin[7], Thao D. Nguyen[4,8], David H. Gracias[2,8†], Lewis H. Romer[1,5,6,9,10†]

Changes in structure and function of small muscular arteries play a major role in the pathophysiology of pulmonary hypertension, a burgeoning public health challenge. Improved anatomically mimetic in vitro models of these microvessels are urgently needed because nonhuman vessels and previous models do not accurately recapitulate the microenvironment and architecture of the human microvascular wall. Here, we describe parallel biofabrication of photopatterned self-rolled biomimetic pulmonary arterial microvessels of tunable size and infrastructure. These microvessels feature anatomically accurate layering and patterning of aligned human smooth muscle cells, extracellular matrix, and endothelial cells and exhibit notable increases in endothelial longevity and nitric oxide production. Computational image processing yielded high-resolution 3D perspectives of cells and proteins. Our studies provide a new paradigm for engineering multicellular tissues with precise 3D spatial positioning of multiple constituents in planar moieties, providing a biomimetic platform for investigation of microvascular pathobiology in human disease.

INTRODUCTION

Dysregulation of vasomotor tone in arterial vessels with lumen diameters in the range of 50 to 300 μm accounts for increased peripheral resistance in major cardiovascular diseases (CVDs) worldwide, including heart disease and pulmonary hypertension (*1*–*3*). By nomenclature convention, the term human "small muscular pulmonary arteries" (hSMPAs) is used to describe supply-side microvascular resistance vessels in the human pulmonary circulation, vessels that are equivalent to arterioles in the systemic circulation (*4*). Currently available in vitro models do not adequately recapitulate the complex structure, microenvironment, and physiological functionality of the smallest human arteries. Despite substantial contributions, animal models of CVD also have limitations due to fundamental differences from human vascular infrastructure (*5*). In addition, there is a push to decrease use of animal models for economic and ethical reasons (*6*).

Microvascular tissue–inspired in vitro models will improve the efficiency with which basic and translational research may advance our understanding of CVD pathophysiology and enhance drug discovery (*7*). Mass-producible biomimetic vessels could also provide investigators with precisely engineered systems with greater potential for customized and personalized medicine applications. However, current in vitro models are tedious to produce, and this hinders progress toward higher-throughput platforms and parallel testing of multiple samples.

Mimicry of native microenvironmental geometry (*8*), surface topography and chemistry (*9*), and surface stiffness (*10*) have gained momentum as appreciation for the impact of these factors on target cell phenotype and gene expression has grown. Plasma membrane curvature modulates signaling cascades through changes in the distribution of transmembrane proteins (*11*), spatial distribution of various organelles, and diffusion rates of metabolites (*12*). Alignment of cells alters protein expression as compared with a randomly ordered baseline (*13*). Changes in the preponderance of individual basement membrane proteins modify cell phenotype in situ and in vitro (*14*). Construction of a functional biomimetic microvasculature has not yet been accomplished despite the production of numerous bioengineered vascular models (*15*–*17*).

Tissue-on-a-chip or organ-on-a-chip systems have integrated cell culture with microfluidics to recapitulate physiological stimuli such as shear stress and cyclic stretch (*18*, *19*) and to facilitate graded exposures of cells to nanoparticles, drugs (*20*), and bacteria. In further advances, organ-level functional replication (*18*), cell migration (*21*), and cell-cell interactions (*22*) have been reproduced in vitro. However, several issues distance currently microfabricated fluidic chips from the goal of reproduction of native microvessel morphometry. Rectangular vessel cross sections with flat sidewalls do not recapitulate natural curvature, and porous polymeric membranes alter diffusion distance for gasotransmitters and other vasoactive effector molecules and may decrease cell-to-cell contact (*23*). Recently reported microfluidic human engineered microvessels lack the patterning and layering of both endothelial cell (EC) and smooth muscle cell (SMC) layers that comprise the microvascular wall (*24*). Alternatively, manually rolled tissue vascular constructs facilitate direct cell-to-cell contact (*17*), but this technique is tedious and would require special machinery for scaled-up production. Barreto-Ortiz *et al.* (*15*) fabricated fibrin hydrogel fiber vascular models; however, the plasmin treatment that was used to produce a lumen had a negative impact on cell viability. Moreover, layering, relative alignment, and uniform deposition of cells on spun fibers can be very challenging to implement.

To address these limitations, we demonstrate the first report of a biomimetic construct that includes essential features of an hSMPA. Human matrix and pulmonary cells were used to achieve anatomically correct layering of intimal ECs and aligned vascular SMCs

[1]Department of Anesthesiology and Critical Care Medicine, Johns Hopkins University School of Medicine, Baltimore, MD, USA. [2]Department of Chemical and Biomolecular Engineering, Johns Hopkins University, Baltimore, MD, USA. [3]Microscope Facility, Johns Hopkins University School of Medicine, Baltimore, MD, USA. [4]Department of Mechanical Engineering, Johns Hopkins University, Baltimore, MD, USA. [5]Department of Biomedical Engineering, Johns Hopkins University School of Medicine, Baltimore, MD, USA. [6]Department of Cell Biology, Johns Hopkins University School of Medicine, Baltimore, MD, USA. [7]Department of Pathology, Johns Hopkins University School of Medicine, Baltimore, MD, USA. [8]Department of Materials Science and Engineering, Johns Hopkins University, Baltimore, MD, USA. [9]Department of Pediatrics, Johns Hopkins University School of Medicine, Baltimore, MD, USA. [10]Center for Cell Dynamics, Johns Hopkins University School of Medicine, Baltimore, MD, USA.
*These authors contributed equally to this work.
†Corresponding author. Email: dgracias@jhu.edu (D.H.G.); lromer@jhmi.edu (L.H.R.)

(VSMCs), with a laminin-based internal elastic lamina. VSMC alignment and growth patterns are a key feature in types of pulmonary hypertension pathogenesis, and our tunable approach to engineering this component of hSMPA cytoarchitecture is essential to both the accurate biomimicry of our model as well as for its applicability for testing and recapitulating pathophysiology (*25*–*27*). We used photolithography and deposition of biocompatible thin films. Strain engineering of bilayered thin films and a sacrificial layer with tunable solubility were harnessed to trigger self-folding of the cell-laden tubes (*28*, *29*). In contrast to prior roll-up strategies, our approach harnesses prerelease patterning of adhesive matrix proteins and nonadhesive poloxamers to enhance fidelity and facilitate precision patterning of human cells. Together with tunable multicellular layering, this enabled us to recapitulate the microarchitecture of the vessel wall. Microvessel lumens formed naturally upon rolling, thus eliminating the need to use an enzymatic process that could decrease cell viability. We validated functionality by measuring cell viability, EC nitric oxide (NO) production, and signaling protein expression. We observed that activation of EC nitric oxide synthase (eNOS) and production of NO were markedly higher in human pulmonary microvascular ECs (HPMECs) grown in biomimetic microvessels than in cells grown on flat surfaces.

RESULTS

Biofabrication of biomimetic hSMPA

We recapitulated key features of hSMPA, including diameters ranging from 50 to 300 μm, a confluent EC intimal lining, and an aligned VSMC population (Fig. 1, A and B) (*30*). SiO/SiO_2 bilayer self-folding films were patterned at wafer scale (Fig. 1C). This includes photolithography, physical vapor deposition, and protein patterning as detailed in Materials and Methods and fig. S1. This process is highly parallel with the capacity to accommodate hundreds to thousands of constructs per wafer (Fig. 1 and figs. S1 and S2). SiO and SiO_2 were selected for use in the tubular constructs because of biocompatibility, optical transparency, and amenability to surface modifications (*28*, *31*, *32*). Mismatched strain in the SiO/SiO_2 bilayer that was formed during film deposition drove the spontaneous folding on dissolution of the sacrificial layer to form three-dimensional (3D) constructs (figs. S1 and S2). By varying the lateral dimensions and thickness of the SiO/SiO_2 bilayer, we were able to fabricate tubes with lengths varying from 0.5 to 3 mm and external diameters from 70 to 300 μm (fig. S2; see Materials and Methods). The SiO_2 is amenable to surface modification, allowing for patterning of matrix proteins on the luminal surface of the tubular constructs (Fig. 1D).

Germanium (Ge) beneath SiO/SiO_2 was used as a cell-friendly sacrificial layer to avoid the need for harsh chemicals during dissolution and biomimetic hSMPA assembly while providing tunable detachment times to enable optimal adhesion of the constituent cell layers (*33*, *34*). GeO_x degrades over time in cell culture media, and its thickness and oxidation are critical for tuning time for lift-off. GeO_x does not induce cellular toxicity (*34*, *35*). We experimented with different deposition and oxidation conditions and chose a 60-nm-thick film oxidized by oxygen plasma treatment at 70 W for 20 s. This resulted in GeO_x dissolution in ~10 hours, which enabled the requisite cell layering to form before roll-up. Uniform cell coverage was achieved, as seen from the actin labeling in EC in Fig. 1E. Cell viability is shown in fig. S2 (calcein-AM).

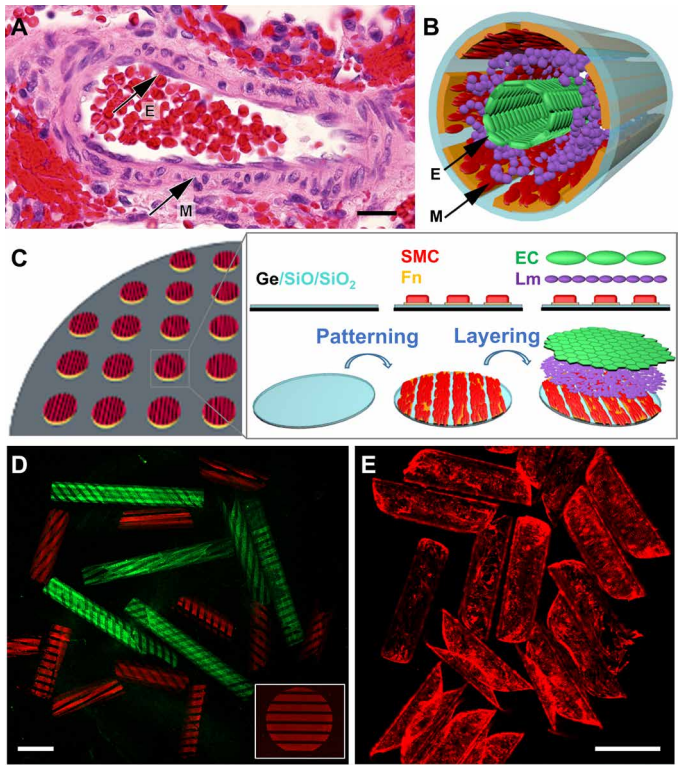

Fig. 1. Schematics and optical images showing biomimetic hSMPA fabrication and structural similarity to a human small muscular distal acinar pulmonary artery. (**A**) Color photomicrograph of an adult hSMPA at the level of the respiratory bronchiole shown in cross section with hematoxylin and eosin staining. Black arrows indicate the EC of the intimal layer (E) and the VSMCs of the muscularis (M). Scale bar, 20 μm. Original magnification, ×200. This native artery exhibits several important structural characteristics including multicellular layering, curvature, and patterning. (**B**) Schematic illustration of the biomimetic hSMPA featuring patterning of cells and layering of VSMCs (M), laminin, and ECs (E). (**C**) Schematic illustration of the highly parallel, multistep patterning and assembly process for biomimetic hSMPA. Germanium (Ge) and bilayers of optically transparent silicon oxide and silicon dioxide (SiO/SiO_2) were deposited on silicon wafers using electron-beam evaporation, followed by adhesive protein patterning and cell layering, which were all achieved in 2D. Upon dissolution of the sacrificial germanium layer in cell culture medium, the 2D bilayer films were released and then self-folded into tubes. Additional fabrication details are shown in the schematic in fig. S1, and snapshots of the roll-up process are shown in fig. S2. Fn, fibronectin; Lm, laminin. (**D**) Confocal microscope images of tubular constructs with tunable 1 and 2 mm length and protein pattern. Luminal surfaces of the tubular constructs were patterned with fluorescently labeled fibronectin (red) or bovine serum albumin (green). The distribution of protein fluorescence intensity is shown in fig. S8A. For cell culture, fibronectin without fluorescence labeling was used. Scale bar, 500 μm. (**E**) Epifluorescence images of rhodamine-phalloidin–labeled ECs growing on the luminal surfaces of biomimetic microvessels. Scale bar, 500 μm.

Mechanical considerations for the tubular constructs

We developed a mechanics model that integrates elastic modulus, substrate thickness, and radius of curvature to study the flexural stiffness that vascular wall cells are exposed to in these tubular constructs. Elastic moduli of SiO and SiO_2 typically exceed that of the native pulmonary arteriolar vessel wall by six orders of magnitude, yet the flexural rigidity on a cellular scale is substantially offset by the use of thin and curved substrates.

To model the flexural stiffness that cells are exposed to, we considered a theoretical model of a thin, long, elastic tube of radius R and thickness $t \ll R$, compressed by two equal and opposite concentrated forces F acting in the radial direction (Fig. 2A). For a linear elastic, isotropic material, the deflection w_0 of the tube directly underneath the applied forces F scales with the Young's modulus E, thickness t, and radius R of the tube as follows on the basis of classical theory (*36*, *37*)

$$w_0 = C\frac{FR^{\frac{3}{2}}}{Et^{\frac{5}{2}}} \quad (1)$$

where C is a proportionality constant. The radius R and thickness t used here are based on our experimental measurements. The Young's modulus E of the silicon substrates used here has been characterized extensively in previous studies (*38*).

We applied finite element analysis to verify the theoretical scaling law and evaluate the proportionality constant $C = 1.173$ for forces representative of cellular traction (Supplementary Materials and fig. S10C). Figure 2A (right) shows a representative deformation when a force of 13.2 μN (which is within the range of reported cell traction forces) was applied to a tube with a thickness of 1.2 μm (*39*). The deflection is enlarged 500 times for visualization (fig. S10B). Equation 2 shows that the flexural stiffness (ψ) experienced by cells exerting forces on a tube

$$\psi = \frac{Et^{\frac{5}{2}}}{1.173\,R^{\frac{3}{2}}} \quad (2)$$

scales with the Young's modulus and thickness as $Et^{5/2}$. Figure 2B demonstrates the design space for the flexural stiffness ψ of tubular structures with thickness varying from 0.5 to 2 μm and Young's modulus varying from 1 to 200 GPa. For in vivo hSMPA, thicknesses of 10 to 30 μm and Young's moduli of 15 to 500 kPa have been reported in the literature (*40*–*43*). The inserted plane in Fig. 2B marks the calculated flexural stiffness of hSMPA based on t = 30 μm and E = 500 kPa. Figure 2C shows the relationship between Young's modulus and thickness for a tubular construct with the same flexural stiffness as in vivo hSMPA (t = 30 μm and E = 500 kPa). It shows that a silica tube (E = 77 GPa) of thickness t ~ 250 nm exhibits the same deflection as a human vessel of the same radius (R = 125 μm) when they are subjected to the same force. The scaling analysis suggests that our SiO/SiO_2 tubular constructs approximate the micromechanics of the hSMPA wall, and this is consonant with the findings of Cavallo *et al.* (*38*), in their examination of thin silicon membranes in the context of cellular contact radii. Furthermore, as silicon oxide degrades in physiological conditions, the flexural stiffness of these thin constructs will more closely approximate the native state with time, and this also enhances the biocompatibility of these materials (*31*, *44*, *45*). Alternative substrate materials with tunable dissolution times exist, and our methodology allows incorporation of these materials in future iterations.

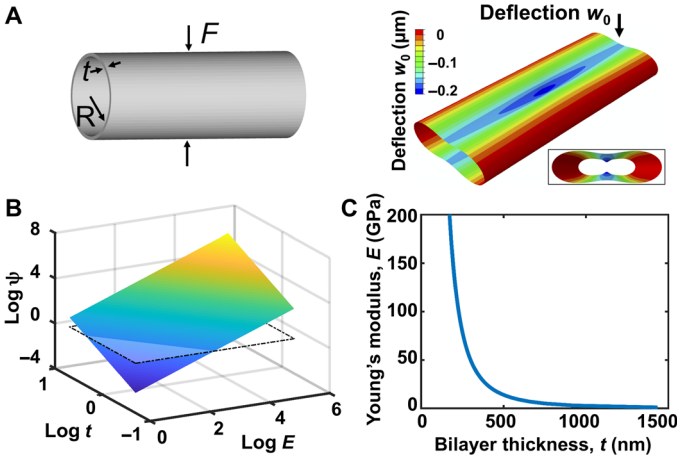

Fig. 2. Micromechanics model illustrating similar flexural stiffness in an ultrathin, high-modulus tube as in a thicker, low-modulus tube. (**A**) Left: Schematic of a thin long elastic tube compressed by two equal and opposite radial loads. Right: Finite element snapshot showing the deflection of the tube when a force of 13.2 μN is applied to a tube with a thickness of 1.2 μm. The inset shows the front view of the deformed cylindrical shell. The deflection was enlarged 500 times for visualization. (**B**) 3D natural log plot of flexural stiffness (ψ; unit: N/m), for tubes with a range of Young's moduli (E; 1 to 200 GPa) and wall thicknesses (t; 0.5 to 2 μm). The inserted plane shows the flexural stiffness calculated on the basis of Eq. 2, using values from hSMPA (t = 30 μm and E = 500 kPa). The plot shows that a tube composed of a thin wall with a high modulus can have the same compliance as a thicker tube with a low modulus. (**C**) Analytical predictions of the combination of the wall thickness (t) and Young's modulus (E) for tubular constructs that yield the same flexural stiffness (ψ) as biological hSMPA (t = 30 μm and E = 500 kPa). The plot illustrates that tubes with wall thicknesses below ~500 nm can be composed of stiff wall materials and yet achieve the same flexural stiffness as thick-walled tubes composed of ultrasoft materials such as hydrogels or the cells and extracellular matrix of native blood vessels.

Characterizing HPMEC monolayer coverage and morphology

A confluent monolayer of HPMEC, with tightly contiguous vascular endothelial (VE)–cadherin–mediated junctions, was visualized on the luminal surface of the biomimetic microvessel 48 hours after cell seeding (Fig. 3; movie S1; and figs. S3A, S4A, and S6). Despite the relative transparency of the SiO/SiO_2 substrate, high-resolution subcellular imaging of the entire 3D biomimetic microvessel is challenging because of the depth of the structure and its curvature, both of which introduce optical aberrations that degrade image quality. We addressed these challenges by using a refractive index–matched mountant, followed by sequential imaging of each of the four sides of the samples by rotation around the central axis. Processing involved correction of axial chromatic aberration, digital straightening, registration by cross-correlation, and final stitching, with the end results consisting of a digitally unrolled Z-stack of the entire tube (fig. S4A). This format was convenient for downstream analysis and 2D visualization and could be projected back onto a cylindrical surface for 3D visualization (please see Materials and Methods and the Supplementary Materials).

Coculture and layering of HPMEC and human pulmonary artery SMC

To recapitulate cell layering in the wall of the hSMPA, human pulmonary artery SMCs (HPASMCs) were seeded on top of the bilayer films, followed by the deposition of laminin, a major component of the inner elastic lamina (*25*), and last, HPMECs. The thickness and oxidation of the sacrificial Ge layer were adjusted to finely tune the lift-off and folding process of the biomimetic hSMPA with both cell layers (HPASMC and HPMEC) after 10 hours (Fig. 4 and figs. S4, S5, and S7A). Distinct and anatomically correct layering of the two cell types were demonstrated by imaging a portion of the tube at

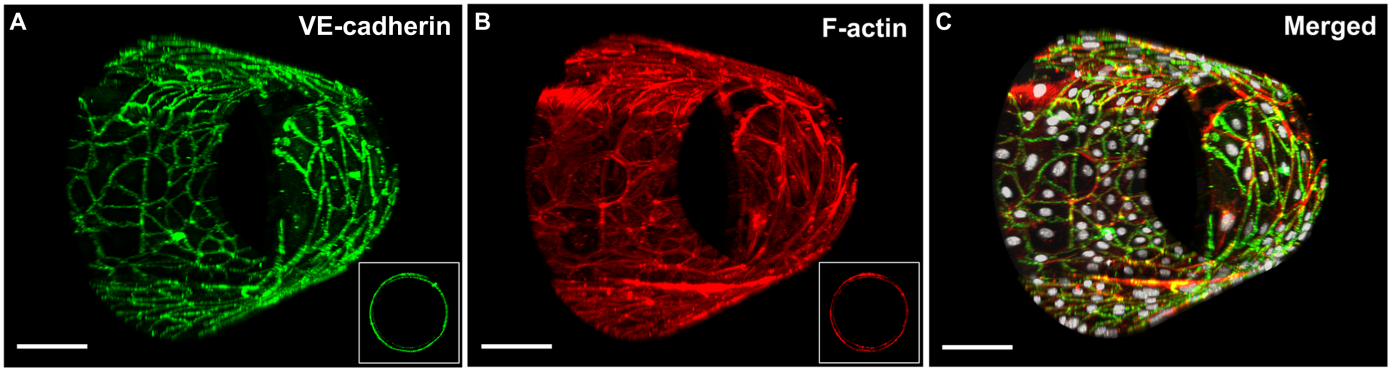

Fig. 3. 3D reconstructions of biomimetic microvessels with ECs illustrating uniformity of cell coverage and intercellular junctional morphology. Reconstructions of confocal *Z*-stacks of biomimetic microvessels populated by HPMECs, featuring the following: (**A**) VE-cadherin at endothelial adherens junctions (antibody labeling, green), (**B**) F-actin (phalloidin, red), and (**C**) merged images that include nuclei [4′,6-diamidino-2-phenylindole(DAPI), gray scale]. Insets in (A) and (B) show the cross-sectional views in the corresponding color channel and demonstrate the amount of overlap due to the roll-up process. Scale bars, 100 μm. A green-magenta rendering of this figure is shown in fig. S6.

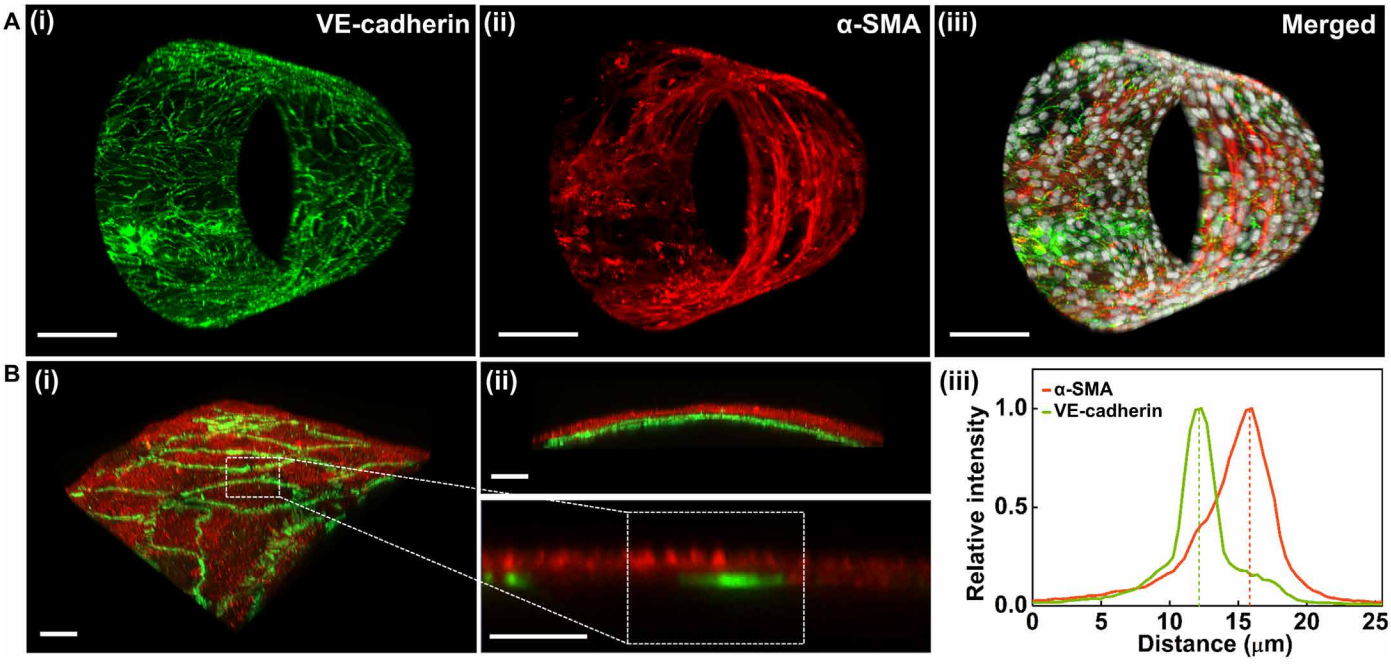

Fig. 4. HPMEC and HPASMC are layered in biomimetic hSMPA. (**A**) Reconstructions of confocal *Z*-stacks of biomimetic hSMPA populated by layered cocultures of HPMEC (luminal) and HPASMC. (i) VE-cadherin (antibody labeling, green), (ii) smooth muscle α-actin (α-SMA) (antibody labeling, red), and (iii) merged image including nuclei from both cell types (DAPI, gray scale). Scale bars, 100 μm. (**B**) (i) 3D view of two-channel confocal imaging of a small region of a biomimetic hSMPA. HPMEC are visualized using anti–VE-cadherin antibody (green), while smooth muscle α-actin antibody labeling (red) shows the HPASMC. (ii) *XZ* projection demonstrates segregation and layering of these two cellular components in this biomimetic hSMPA. The bottom panel in (ii) is sampled from (i) and exhibits intensity distribution. Scale bars, 20 μm. (iii) Normalized fluorescence intensity is plotted versus relative radial distance from the tube's lumen. The distance between the two cell layers is approximately 3.5 μm. A green-magenta rendering of this figure is shown in fig. S7.

higher resolution. Figure 4B and fig. S7B show a representative image of cocultured cells in the biomimetic hSMPAs. The segregation of cell populations can be clearly observed from the side view: Abluminal smooth muscle α-actin (red, magenta in fig. S7) and luminal VE-cadherin (green) were documented [Fig. 4B and fig. S7B (i to iii)]. Spatial mapping of fluorescence signal intensity demonstrated a separation of approximately 3.5 μm between the peaks of the two fluorophores (the *Z* dimension was enlarged for visualization in fig. S8E; see also movie S2; a flat, stitched image of the cocultured tube is shown in fig. S4B).

Alignment of HPASMC by patterning fibronectin

VSMCs in the medial layer of hSMPAs are oriented in a circumferential fashion with a diagonal alignment relative to the long axis of

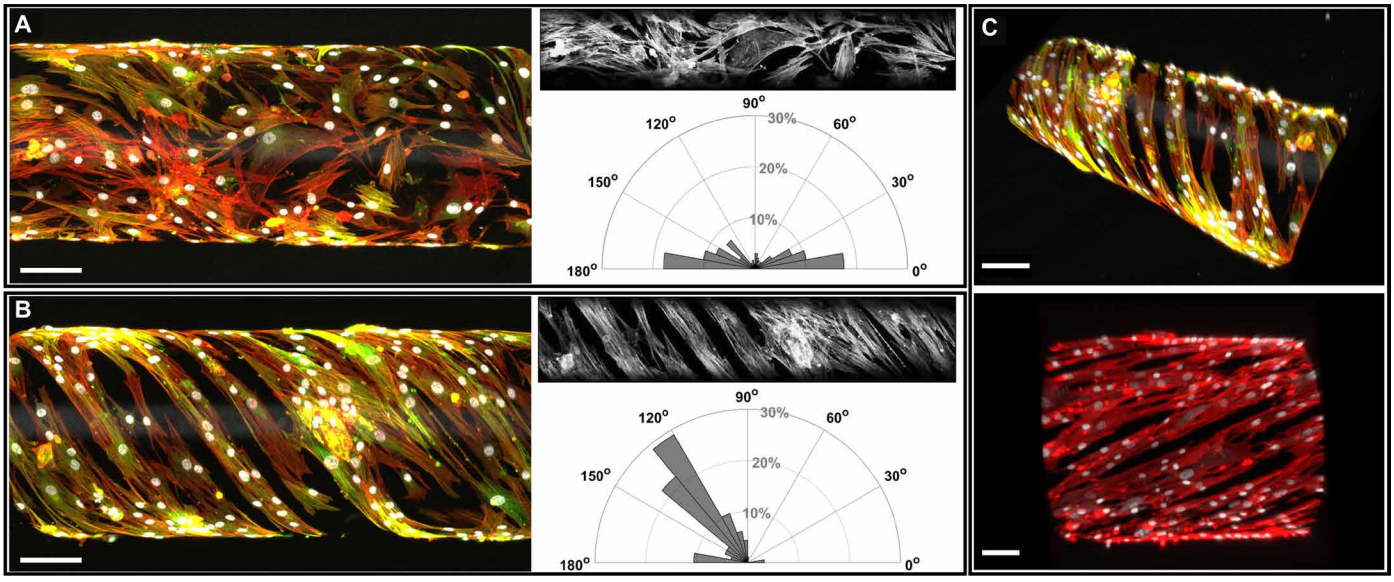

Fig. 5. Patterned fibronectin on tubular constructs oriented HPASMC adhesion. (**A**) Confocal image (side view) of HPASMCs on an unpatterned tubular construct, stained for F-actin (phalloidin, red), smooth muscle α-actin (antibody labeling, green), and nuclei (DAPI, gray scale). The polar plot is based on image analysis of the gray scale F-actin image and shows that without patterning, HPASMCs attached and spread with random orientation. (**B**) Confocal image (side view) of HPASMCs grown on a patterned tubular construct, stained for F-actin (phalloidin, red), smooth muscle α-actin (antibody labeling, green), and nuclei (DAPI, gray scale). On the basis of image analysis of the gray scale F-actin image, the polar plot shows that F-actin filaments demonstrated alignment in parallel helical structures on the fibronectin-patterned scaffold. Binning in the polar plots is 10°. (**C**) 3D views of biomimetic microvessels demonstrating tunable variations in orientation angles and patterning periodicity, with labeled F-actin (phalloidin, red), smooth muscle α-actin (antibody labeling, green), and nuclei (DAPI, gray scale). Scale bars in (A to C), 100 μm.

the vessel (*25*–*27*). This alignment and the extent to which VSMCs populate distal portions of acinar arteries have a profound effect on pulmonary microvascular flow and vasoreactivity. Models that do not capture this alignment or allow for tunability in pitch and orientation fail to address this important issue in hSMPA cytoarchitecture and its ramifications for pulmonary vascular resistance. To recapitulate this alignment, lithography was used to pattern fibronectin on the films (before release and rolling) and the integrity of the pattern was preserved after self-assembly of the biomimetic microvessels (fig. S8, A and B). HPASMCs cultured on these surfaces exhibited high fidelity and anatomically correct cell alignment as quantified by image analysis of F-actin (fig. 5B). These results contrasted with the random pattern of adhesion seen in HPASMCs that were grown on unpatterned substrates (Fig. 5A). Since individual SiO/SiO_2 films roll up in random orientations upon lift-off from the substrate, the orientation of patterned fibronectin will align differently with regard to the tube folding direction in each biomimetic microvessel or hSMPA (Fig. 1D). In future work, controlled directionality of patterning can be introduced by adding boundary conditions to determine film rolling directions. Furthermore, the widths of both adhesive and nonadhesive regions can be tuned during the 2D patterning via mask design. Figure 5C demonstrates variations in pitch and orientation that were achieved with this approach.

Marked improvement in cellular longevity and signaling in biomimetic hSMPA

Long-term cell viability is an important consideration in tissue engineering. When cocultured in biomimetic hSMPA, both HPMECs and HPASMCs demonstrated substantial improvement in longevity over control cells in flat culture, with >90% viability at day 14 (Fig. 6A and fig. S9A). Furthermore, HPMECs in biomimetic microvessels demonstrated substantial nitric oxide (NO) production as indicated by DAF-DA (4,5-Diaminofluorescein diacetate) labeling (fig. S9C). For quantitative analysis, samples of culture media were collected from biomimetic vessels seeded with only ECs and analyzed by a Sievers NO analyzer. Data shown in Fig. 6B demonstrate that NO production over 48 hours was increased fourfold in HPMECs in biomimetic microvessels, as compared to control cells cultivated on flat SiO/SiO_2 films. Data were analyzed from four sets of (vessels versus flat) samples ($P < 0.01$). To elucidate molecular mechanisms that may drive the increased NO production that we observed in the biomimetic microvessels, activating phosphorylation events in eNOS and protein kinase B (Akt) were examined (*46*–*48*). HPMECs in biomimetic microvessels exhibited augmented phosphorylation of eNOS at Ser^{1177} as compared with control HPMECs on flat films, whereas total eNOS remained unchanged in both culture conditions (Fig. 6C). Densitometry data were analyzed from seven independent experiments ($P < 0.01$). We also observed a trend toward up-regulation of Akt phosphorylation at Thr^{308} in five independent experiments (fig. S9D). These data indicate that the biomimetic hSMPAs described here enhance robust function of vascular wall cells.

DISCUSSION

Our novel strategy for production of self-folding, patterned, multiple cell–layered, 3D biomimetic hSMPA harnesses innovative strain engineering with an approach that is highly reproducible, amenable to high-throughput processing, versatile, tunable, and scalable. Moreover, HPMEC in these biomimetic vessels demonstrated greatly improved eNOS phosphorylation and nitric oxide production as compared with controls from planar cultures, as well as augmented longevity.

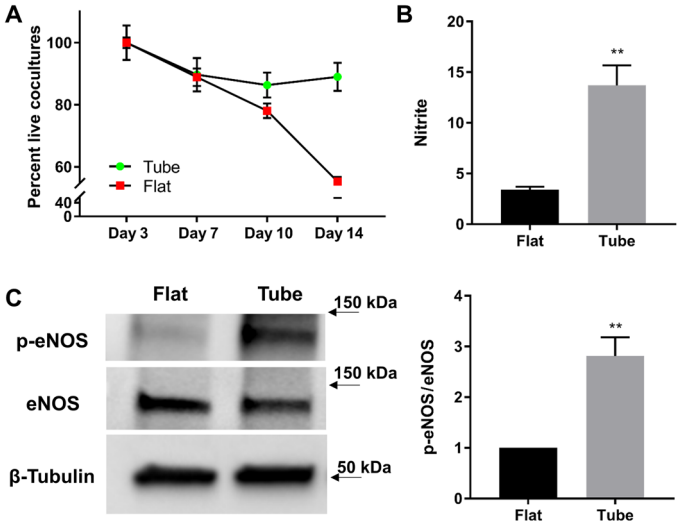

Fig. 6. Cellular longevity and cell signaling demonstrated markedly improved functionality in biomimetic hSMPAs. (**A**) Cell viability was calculated as the percentage of live cells compared with baseline (day 3) using the CyQUANT assay. Coculture of HPMEC and HPASMC populations were assayed. Data from flat (red) and tubular constructs (green) were compared. Data are displayed as means ± SEM. (**B**) HPMECs in the biomimetic microvessels exhibited a fourfold rise in nitric oxide production over the levels observed in HPMEC monolayers in flat culture. Nitrite levels in cell culture medium were determined by using a Sievers bioluminescence nitric oxide analyzer. Nitrite levels were normalized to total protein content for each sample. The numbers in the *y* axis indicate picomoles of nitrite per micrograms of protein. Medium was collected 48 hours after confluency and medium replacement. Data are displayed as means ± SEM (**$P < 0.01$). (**C**) Phosphorylation of eNOS (at Ser^{1177}) was found to be greater in HPMECs that were seeded and cultured on biomimetic microvessels than that in cells on flat SiO/SiO_2 films. HPMECs were grown at each condition for 48 hours. Western blots of cell lysates from each population were analyzed with antibodies against phosphorylated eNOS (p-eNOS), total eNOS, and β-tubulin (protein loading control). Data are displayed as means ± SEM (**$P < 0.01$).

Pulmonary hypertension is a rapidly growing health threat in North America, Europe, and worldwide, and well-articulated expert opinions in the field attest to the inadequacy of animal models for definition of new molecular targets for modifying and reversing disease progression and to the need to move toward diagnostic and drug testing platforms that are based on human tissue (*49*, *50*). The biomimetic hSMPA described here represent an answer to an urgent unmet need by providing a means to achieve real-time functional assessment of biomimetic human arteries without the need for biopsies or human subject testing.

Our biomimetic artery design incorporates important features of native hSMPAs, in which VSMCs and intimal ECs work in close concert. Both signals from EC and VSMC growth patterns and reactivity determine luminal diameter and, thereby, resistance to flow. In native blood vessels, ECs form a monolayer contiguous to the lumen, the intima, that is in direct contact with blood flow. Maintenance of an intact monolayer is vital for the maintenance of a nonthrombotic surface and for immune barrier integrity (*51*). VSMCs in the tunica media of native blood vessels are circumferentially aligned to the vessel axis. VSMC alignment profoundly affects the protein expression of SMC contractile markers and may be linked to disease progression in pulmonary hypertension (*26*, *27*, *52*, *53*). Currently available synthetic blood vessel platforms use a range of creative strategies and yet have numerous limitations. Fabrication techniques often limit their products to large vessel models and applications, and many of these lack microenvironmental features of the smallest human arteries, especially vitally important VSMC alignment (*27*). Microdevices that recapitulate vascular functions in on-chip modules often lack the mechanics and 3D geometry of native blood vessels that have been shown to enhance physiologically accurate phenotypes and to extend viability (*54*, *55*). ECs cultured in conditions that mimic geometric curvature of an arteriole have been shown to exhibit cytoskeletal protein distribution similar to those in vivo tissues, and curvature may also affect SMC phenotype and motility (*56*). Furthermore, monoculture of ECs or SMCs has been accomplished in various scaffolds in the past, but these approaches sacrifice the substantial physiologic synergy between the two cell populations that is integral to microvascular function (*57*). ECs affect SMC morphology, proliferation, and specific priorities in protein synthesis (*58*). Reciprocally, SMCs affect EC production of key vasoactive compounds such as nitric oxide and endothelin-1 (*59*).

In light of these critical biological nuances, we report the development of mass-producible, tunable, self-folding, tubular constructs that incorporate multicellular layering and precise alignment of SMCs while demonstrating notably enhanced viability and functionality of human pulmonary vascular cells. Our approach allows for gradual evolution of self-folding, and this facilitated serial incorporation of multiple cell and matrix layers into these biomimetic vessels. Varying design parameters, we were able to fabricate tubes with lengths varying from 0.5 to 3 mm and external diameters from 70 to 300 μm in this study. The diameters of the tube were tuned by the stress and film thickness, and the length of the tube was adjusted by the 2D film dimension. Further development of this model system will address overlap regions in the biomimetic arterial wall with optimized 2D film shape and lateral dimensions, as well as enhancement of mural remodeling by endothelial outgrowth to achieve an intact single-layer vascular wall. Longevity of optimal cellular function is a factor that limits the practical utility of many cell-based devices. We have demonstrated that the vascular wall cells under study performed and thrived at a higher level in the biomimetic hSMPA than in flat, 2D culture (Fig. 6). Furthermore, since pulmonary EC-derived nitric oxide is essential to the homeostasis of cyclic guanosine monophosphate in pulmonary VSMCs (*3*), improved HPMEC NO production in these biomimetic constructs (Fig. 6) demonstrates an important prerequisite for a diagnostic or drug testing platform for pulmonary hypertension. The enzyme responsible for NO production, eNOS, is activated by phosphorylation of its Ser at residue 1177 by Akt (protein kinase B) in human cells (*47*). In our study, phosphorylation of eNOS was augmented by tubular geometry, and data were controlled by keeping both the total surface area seeded with cells and the protein loading constant for the assays shown. Further interrogation as to how curved geometry affects NO production and its corresponding molecular signaling is needed. Several cellular curvature-sensing proteins such as the BAR family (Bin, amphiphysin, and Rvs161/167) are arc-shaped proteins that adapt to highly curved membranes (*60*). The precise engineering and tunability of our biomimetic vessel production approach may facilitate more exacting interrogation of these molecular mechanisms of endothelial geometry sensing and their contributions to disease pathogenesis and severity.

High-resolution microscopy of hybrid cellular and biomaterial devices with curved 3D topography (such as organoids and organ-on-a-chip

systems) is challenging. Axial (*Z*) resolution in most microscope objectives is considerably lower than lateral (*XY*) resolution. This leads to large variations in feature preservation depending on each cell's orientation, but the curved surfaces of the sample itself refract light, causing aberrations that further degrade image quality with depth. These challenges were addressed in the current study by innovation in both image acquisition and image processing that may facilitate imaging of 3D cultured tissue and organoids in many other settings.

In summary, we have described the first integrated approach to patterning, generating, imaging, and analyzing microaligned and layered cellular and tissue-level function in biomimetic in vitro hSMPAs. Unique design features, cellular performance, and tunability of these biomimetic hSMPAs will be readily translatable to studies of pulmonary hypertension pathobiology, including the impact of VSMC misalignment or overgrowth, altered matrix composition, failure of juxtacrine signaling between ECs and VSMCs, and EC overgrowth. In addition, these constructs are adaptable tools that could be leveraged for drug screening for a number of other diseases in which microvascular function is a factor in pathogenesis and therapeutic drug targeting. The work presented here represents an important step toward an in vitro platform for the study of vascular wall biology and arteriolar fluid mechanics in an anatomically correct and human tissue–specific context-insights that could pave the way to new approaches to ischemic heart disease, stroke, diabetic vasculopathy, and other pressing priorities in medicine worldwide.

MATERIALS AND METHODS

Ex vivo section labeling

A specimen of a normal area of lung in a patient with a congenital pulmonary airway malformation but without pulmonary hypertension was fixed in 10% buffered formalin and processed for paraffin embedding by standard techniques. The cut sections were stained with hematoxylin and eosin.

Tubular construct fabrication

Circular patterns were prepared by photolithography using photoresist Microposit S1827 (MicroChem), ultraviolet (UV) exposure, and Microposit MF 319 developer (MicroChem). Germanium (Ge; Alfa Aesar) was deposited using physical vapor deposition as the sacrificial layer. The Ge surface was oxidized to form germanium oxide (GeO_x) by oxygen plasma treatment (Plasma Etch Inc., model no. PE-100). Next, silicon monoxide (SiO) and silicon dioxide (SiO_2) (Kurt J. Lesker Company) films were deposited using electron-beam evaporation at a rate of 5.5 and 1.5 Å/s, respectively. After deposition, the remaining photoresist was lifted off in acetone and isopropanol. Tubes with diameter of 300 μm were achieved with 500 nm of SiO and 700 nm of SiO_2.

Tubular construct surface modification

The patterned films were modified by cleaning, submerging in 5% APTES [(3-aminopropyl)triethoxysilane; Sigma-Aldrich] in acetone solution for 1 hour, rinsing with acetone and isopropanol, and submerging in 5% glutaraldehyde (Electron Microscopy Sciences) in deionized water for 1 hour. The films were then sterilized in 70% ethanol for 30 min, rinsed using phosphate-buffered saline (PBS) (Life Technologies), and incubated with fibronectin (25 μg/ml; Thermo Fisher Scientific) solution in PBS for 1 hour at 37°C. The films were then rinsed in PBS for three times before cell seeding.

Cell lines and in vitro culture conditions

HPMECs and human pulmonary artery SMCs (HPASMC) (PromoCell) were cultured in their respective cell culture medium (PromoCell), supplemented with 1% penicillin/streptomycin (100 U/100 μg/ml; Life Technologies) at 37°C with 5% CO_2. Tubular constructs coated with fibronectin were placed in sterile Petri dishes. Cells suspended in culture media were transferred onto the substrate at a density of 2×10^5 to 3×10^5 cells/cm^2 for HPASMCs and 4×10^5 cells/cm^2 for HPMECs. For coculture, HPASMCs were first seeded onto the films. After 5 hours, floating HPASMCs were removed, and the underlying layer of HPASMCs was covered with laminin (100 μg/ml; Sigma-Aldrich) for 1 hour at 37°C. The samples were then washed with PBS three times and seeded with HPMECs. A mixture of medium was used for the cocultured cells. After ~10 hours of culture, bilayer films started to release from the wafer and exhibited a tubular shape with layered cells on the luminal side of the tubes.

Live cell and fluorescence confocal imaging

Before immunostaining, cells were permeabilized for 2 min at room temperature in 0.5% Triton X-100 (Sigma-Aldrich) in 4% paraformaldehyde solution. Cells were then washed three times with PBS, incubated in 4% paraformaldehyde solution for 20 min at room temperature, and then probed with fluorophore-tagged antibodies. Samples were incubated with antibodies targeting VE-cadherin (Cayman Chemical, rabbit; 1:100) and smooth muscle α-actin (Santa Cruz Biotechnology, mouse; 1:25) prepared in blocking buffer (0.1% bovine serum albumin in universal buffer) for 1 hour in 37°C. Samples were then incubated in secondary antibody (Alexa Fluor 488 anti-rabbit secondary antibody or Cy3 anti-mouse secondary antibody, Jackson ImmunoResearch; 1:100 dilution) for 1 hour in 37°C. A Zeiss LSM 780 or a Zeiss LSM 800 laser scanning confocal microscope was used for confocal imaging. Cell viability was measured using calcein-AM and ethidium homodimer-1 staining and imaged with a Zeiss LSM 780.

Confocal imaging and 3D reconstruction of biomimetic hSMPA

To image the biomimetic hSMPA, a fixed and stained specimen was first immersed in a low-viscosity, refractive index–matched UV curing adhesive (Norland Products, no. 74) and inserted into a square glass capillary tube with inside dimension of 400 μm (VitroCom, no. 8240-050) to allow close optical access from four directions. The adhesive was solidified with a brief pulse of UV, immobilizing the tube. A Zeiss Plan-Apochromat 20×/0.8 air or Zeiss LD LCI Plan-Apochromat 25×/0.8 multi-immersion objective on a Zeiss LSM 800 confocal microscope was used for all 3D imaging. A 3D-printed rotary device was used to mount the sample and hold it on the microscope stage, which allowed the capillary to be freely rotated around its central axis for sequential imaging of each side, while constraining the other two rotational and three translational degrees of freedom. This approach minimized registration error, while also allowing each face of the tubular construct to face the objective directly, ensuring that each quadrant of cells was aligned along the high-quality *XY* plane and was not occluded by the rest of the tube. *Z*-stacks were obtained for each of the four quadrants sequentially, with a depth sufficient to ensure overlap between adjacent quadrants. The four resulting image stacks were then registered and stitched using a multistage process. First, axial chromatic aberration was corrected by applying a *Z*-offset to the 4′,6-diamidino-2-phenylindole

(DAPI) and Alexa Fluor 488 channels. Next, the axis of the tube within each *Z*-stack was determined, and the stacks were rotated and translated as necessary to achieve a common reference frame around this axis. Next, the curved surface in each stack was digitally straightened using ImageJ (National Institutes of Health) to digitally convert curved surfaces into flattened *Z*-stacks, followed by alignment of overlapping regions. This allowed automatic stitching by ImageJ. Next, final registration was achieved by cross-correlation of the overlapping regions in *X*, *Y*, and *Z* dimensions. Stitching involved excluding the lower quality slices within the overlapping regions and then linearly blending the remaining overlapping voxels to achieve a seamless transition. Last, the complete stitched image was projected back to a cylindrical surface by MATLAB (MathWorks) and exported as a new stack. 3D rendering and projections were visualized in Imaris (Bitplane). To demonstrate the layering of EC and SMC, a higher *Z*-resolution was required, which necessitated using a higher numerical aperture objective. Therefore, a *Z*-stack of a representative region of the tube was obtained using a Zeiss Plan-Apochromat 63×/1.4 oil objective and visualized in Imaris without further processing.

Quantifying endothelial NO production

Live cell nitric oxide production was visualized using DAF-DA staining as per the manufacturer's instructions (Life Sciences). Briefly, cells in the tubular construct were loaded with DAF-DA (5 μM) for 30 min, washed three times with PBS, and incubated for another 30 min in phenol-free media. Fluorescence was determined using a Zeiss LSM 780 confocal microscope. Production of nitric oxide (NO) was quantified using a Sievers 280i NO analyzer for HPMEC cultured alone in biomimetic microvessels. NO produced by cells in the culture medium is rapidly oxidized to nitrite (NO_2^-). NO_2^- in the media was measured from tube and flat culture mediums and injected in glacial acetic acid–containing potassium iodide in the reaction chamber. NO_2 is quantitatively reduced to NO under these conditions, which was quantified by a chemiluminescence detector after reaction with ozone. The NO production was normalized by the total protein amount from the sample where the NO was collected. The protein was quantified from cell lysates using a Pierce Coomassie (Bradford) protein assay kit (Thermo Fisher Scientific).

Cell viability

Cell viability in our tubular constructs was ascertained using the CyQUANT Cell Proliferation Assay (Sigma-Aldrich). EC, SMC, or cocultures were seeded on flat or tubular constructs. Three parallel replicates were collected from each cell type cultivated in both flat and tubular conditions at corresponding times on days 3, 7, 10, and 14. Cells were trypsinized from the flat or tubular scaffolds and collected by centrifuge. The cell pellet was then analyzed using CyQUANT assay as per the manufacturer's protocol. The DNA amount was used as indicator for cell number. All readings were normalized to the values obtained at day 3.

Immunoblotting

Cells were harvested from their respective culture conditions in lysis buffer containing 0.1% deoxycholate, 0.1% Triton X-100, 2 μM EDTA, 2 mM sodium orthovanadate, leupeptin (20 μg/ml), and aprotinin (20 μg/ml) in universal buffer. Cell lysates were clarified by sonication and centrifugation at 15,000*g* at 4°C for 10 min, and lysate volumes were normalized for equal protein content using Coomassie protein assay (Pierce). Equal amounts of protein (with a range of 1 to 5 μg) were loaded per lane to a 4 to 15% SDS–polyacrylamide gel electrophoresis gel (Bio-Rad) at 200 V for 35 min. Proteins were then electroblotted onto nitrocellulose membranes (Bio-Rad). Blots were then blocked with 5% milk (Bio-Rad) in TBST (0.2% Tween 20 in 1× tris-buffered saline) and followed by incubation in the following primary antibodies: anti–phospho-eNOS (Ser^{1177}) (Cell Signaling Technology, rabbit; 1:1000), anti-eNOS (Santa Cruz Biotechnology, mouse; 1:500), anti–phospho-Akt (Thr^{308}) (Cell Signaling Technology, rabbit; 1:2000), anti-Akt (Cell Signaling Technology, rabbit; 1:1000), and anti–β-tubulin (Abcam, rabbit; 1:3000).

Surface patterning for SMC alignment

We used photolithography to pattern proteins. Thoroughly cleaned substrates were first coated with hexamethyldisilazane by vapor deposition before spin-coating with S1805 photoresist. The samples were patterned with arrays of lines (20 to 100 μm wide) separated by 50 μm spaces. The substrates were then serially incubated with APTES vapor (1 hour) and 5% glutaraldehyde solution (1 hour) and then sterilized and incubated with fibronectin solution (25 μg/ml) for 1 hour at 37°C to allow the protein to bind with the surface. The remaining photoresists were removed by swiftly rinsing in acetone and isopropanol. The substrates were sterilized and then submerged in sterile 1% Pluronic®F-127 (Sigma-Aldrich) for 30 min. After incubation, substrates were washed with 1× PBS to remove residual Pluronic® solution. The substrates were then immediately seeded with SMCs.

Statistical analysis

Statistical analyses were performed using Prism (GraphPad software). Data are presented as means ± SEM. A two-tailed *t* test was used to analyze the data for statistical significance. Information for *N* and for *P* values is included with each individual data presentation in Results or the figure legends.

SUPPLEMENTARY MATERIALS

Supplementary material for this article is available at http://advances.sciencemag.org/cgi/content/full/6/13/eaaz2598/DC1

Supplementary Methods

Fig. S1. A schematic illustration of detailed fabrication process.

Fig. S2. Self-folding of silicon monoxide and silicon dioxide bilayer films.

Fig. S3. ECs and SMCs form a monolayer in biomimetic microvessels.

Fig. S4. Cells on the luminal surface of the tube (digitally unrolled).

Fig. S5. Biomimetic microvessel populated by cocultured HPMEC and HPASMC, cross-sectional and en face views.

Fig. S6. Green-magenta version of data in Fig. 3: 3D reconstructions of biomimetic microvessels with ECs illustrating uniformity of cell coverage and intercellular junctional morphology.

Fig. S7. Green-magenta version of data in Fig. 4: HPMECs and HPASMCs are layered in biomimetic hSMPA.

Fig. S8. SMC patterning and layering of multiple cell types.

Fig. S9. Cell longevity and HPMEC function studies.

Fig. S10. Finite element study details.

Movie S1. Video for 3D view of hSMPA populated by HPMECs.

Movie S2. Video for 3D view of hSMPA populated by coculture of HPMEC and HPASMCs.

View/request a protocol for this paper from *Bio-protocol*.

REFERENCES AND NOTES

1. J. C. Frisbee, D. W. Stepp, Impaired NO-dependent dilation of skeletal muscle arterioles in hypertensive diabetic obese Zucker rats. *Am. J. Physiol. Heart Circ. Physiol.* **281**, H1304–H1311 (2001).
2. H. D. Intengan, E. L. Schiffrin, Structure and mechanical properties of resistance arteries in hypertension: Role of adhesion molecules and extracellular matrix determinants. *Hypertension* **36**, 312–318 (2000).

3. C. Unegbu, C. Noje, J. D. Coulson, J. B. Segal, L. Romer, Pulmonary hypertension therapy and a systematic review of efficacy and safety of PDE-5 inhibitors. *Pediatrics* **139**, e20161450 (2017).
4. A. A. Hislop, C. M. Pierce, Growth of the vascular tree. *Paediatr. Respir. Rev.* **1**, 321–328 (2000).
5. H. G. Tsang, N. A. Rashdan, C. B. A. Whitelaw, B. M. Corcoran, K. M. Summers, V. E. MacRae, Large animal models of cardiovascular disease. *Cell Biochem. Funct.* **34**, 113–132 (2016).
6. S. Festing, R. Wilkinson, The ethics of animal research. Talking point on the use of animals in scientific research. *EMBO Rep.* **8**, 526–530 (2007).
7. K. E. Bailey, M. L. Floren, T. J. D'Ovidio, S. R. Lammers, K. R. Stenmark, C. M. Magin, Tissue-informed engineering strategies for modeling human pulmonary diseases. *Am. J. Physiol. Lung Cell. Mol. Physiol.* **316**, L303–L320 (2019).
8. J. V. Serbo, S. Kuo, S. Lewis, M. Lehmann, J. Li, D. H. Gracias, L. H. Romer, Patterning of fibroblast and matrix anisotropy within 3D confinement is driven by the cytoskeleton. *Adv. Healthc. Mater.* **5**, 146–158 (2016).
9. D. M. Brunette, B. Chehroudi, The effects of the surface topography of micromachined titanium substrata on cell behavior in vitro and in vivo. *J. Biomech. Eng.* **121**, 49–57 (1999).
10. D. E. Discher, P. Janmey, Y.-L. Wang, Tissue cells feel and respond to the stiffness of their substrate. *Science* **310**, 1139–1143 (2005).
11. S. Aimon, A. Callan-Jones, A. Berthaud, M. Pinot, G. E. S. Toombes, P. Bassereau, Membrane shape modulates transmembrane protein distribution. *Dev. Cell* **28**, 212–218 (2014).
12. C. Wilson, C. D. Saunter, J. M. Girkin, J. G. McCarron, Pressure-dependent regulation of Ca2+ signalling in the vascular endothelium. *J. Physiol.* **593**, 5231–5253 (2015).
13. T. Fee, S. Surianarayanan, C. Downs, Y. Zhou, J. Berry, Nanofiber alignment regulates NIH3T3 cell orientation and cytoskeletal gene expression on electrospun PCL+Gelatin nanofibers. *PLOS One* **11**, e0154806 (2016).
14. J. U. G. Wagner, E. Chavakis, E.-M. Rogg, M. Muhly-Reinholz, S. F. Glaser, S. Günther, D. John, F. Bonini, A. M. Zeiher, L. Schaefer, M.-J. Hannocks, R. A. Boon, S. Dimmeler, Switch in laminin β2 to lminin β1 isoforms during aging controls endothelial cell functions—brief report. *Arterioscler. Thromb. Vasc. Biol.* **38**, 1170–1177 (2018).
15. S. F. Barreto-Ortiz, J. Fradkin, J. Eoh, J. Trivero, M. Davenport, B. Ginn, H. Q. Mao, S. Gerecht, Fabrication of 3-dimensional multicellular microvascular structures. *FASEB J.* **29**, 3302–3314 (2015).
16. X. Cui, T. Boland, Human microvasculature fabrication using thermal inkjet printing technology. *Biomaterials* **30**, 6221–6227 (2009).
17. R. Gauvin, T. Ahsan, D. Larouche, P. Lévesque, J. Dubé, F. A. Auger, R. M. Nerem, L. Germain, A novel single-step self-assembly approach for the fabrication of tissue-engineered vascular constructs. *Tissue Eng. Part A* **16**, 1737–1747 (2010).
18. D. Huh, B. D. Matthews, A. Mammoto, M. Montoya-Zavala, H. Y. Hsin, D. E. Ingber, Reconstituting organ-level lung functions on a chip. *Science* **328**, 1662–1668 (2010).
19. H. J. Kim, D. E. Ingber, Gut-on-a-Chip microenvironment induces human intestinal cells to undergo villus differentiation. *Integr. Biol.* **5**, 1130–1140 (2013).
20. Y. C. Toh, T. C. Lim, D. Tai, G. Xiao, D. van Noort, H. Yu, A microfluidic 3D hepatocyte chip for drug toxicity testing. *Lab Chip* **9**, 2026–2035 (2009).
21. F.-Q. Nie, M. Yamada, J. Kobayashi, M. Yamato, A. Kikuchi, T. Okano, On-chip cell migration assay using microfluidic channels. *Biomaterials* **28**, 4017–4022 (2007).
22. Y. Gao, D. Majumdar, B. Jovanovic, C. Shaifer, P. C. Lin, A. Zijlstra, D. J. Webb, D. Li, A versatile valve-enabled microfluidic cell co-culture platform and demonstration of its applications to neurobiology and cancer biology. *Biomed. Microdevices* **13**, 539–548 (2011).
23. C. S. Wallace, G. A. Truskey, Direct-contact co-culture between smooth muscle and endothelial cells inhibits TNF-alpha-mediated endothelial cell activation. *Am. J. Physiol. Heart Circ. Physiol.* **299**, H338–H346 (2010).
24. W. J. Polacheck, M. L. Kutys, J. B. Tefft, C. S. Chen, Microfabricated blood vessels for modeling the vascular transport barrier. *Nat. Protoc.* **14**, 1425–1454 (2019).
25. M. I. Townsley, Structure and composition of pulmonary arteries, capillaries, and veins. *Compr. Physiol.* **2**, 675 (2012).
26. P. Davies, L. Reid, Hypoxic remodeling of the rat pulmonary arterial microcirculation assessed by microdissection. *J. Appl. Physiol. (1985)* **71**, 1886–1891 (1991).
27. P. Davies, G. Burke, L. Reid, The structure of the wall of the rat intraacinar pulmonary artery: An electron microscopic study of microdissected preparations. *Microvasc. Res.* **32**, 50–63 (1986).
28. R. Arayanarakool, A. K. Meyer, L. Helbig, S. Sanchez, O. G. Schmidt, Tailoring three-dimensional architectures by rolled-up nanotechnology for mimicking microvasculatures. *Lab Chip* **15**, 2981–2989 (2015).
29. S. Zakharchenko, E. Sperling, L. Ionov, Fully biodegradable self-rolled polymer tubes: A candidate for tissue engineering scaffolds. *Biomacromolecules* **12**, 2211–2215 (2011).
30. E. L. Schiffrin, Reactivity of small blood vessels in hypertension: Relation with structural changes state of the art lecture. *Hypertension* **19** (2 Suppl), II1–II9 (1992).
31. K. Malachowski, M. Jamal, Q. Jin, B. Polat, C. J. Morris, D. H. Gracias, Self-folding single cell grippers. *Nano Lett.* **14**, 4164–4170 (2014).
32. K. J. Yu, D. Kuzum, S.-W. Hwang, B. H. Kim, H. Juul, N. H. Kim, S. M. Won, K. Chiang, M. Trumpis, A. G. Richardson, H. Cheng, H. Fang, M. Thompson, H. Bink, D. Talos, K. J. Seo, H. N. Lee, S.-K. Kang, J.-H. Kim, J. Y. Lee, Y. Huang, F. E. Jensen, M. A. Dichter, T. H. Lucas, J. Viventi, B. Litt, J. A. Rogers, Bioresorbable silicon electronics for transient spatiotemporal mapping of electrical activity from the cerebral cortex. *Nat. Mater.* **15**, 782–791 (2016).
33. C. C. Bufon, C. C. B. Bufon, J. D. C. González, D. J. Thurmer, D. Grimm, M. Bauer, O. G. Schmidt, Self-assembled ultra-compact energy storage elements based on hybrid nanomembranes. *Nano Lett.* **10**, 2506–2510 (2010).
34. Q. Jin, M. Li, B. Polat, S. K. Paidi, A. Dai, A. Zhang, J. V. Pagaduan, I. Barman, D. H. Gracias, Mechanical trap surface-enhanced raman spectroscopy for three-dimensional surface molecular imaging of single live cells. *Angew. Chem. Int. Ed. Engl.* **56**, 3822–3826 (2017).
35. S.-K. Kang, G. Park, K. Kim, S.-W. Hwang, H. Cheng, J. Shin, S. Chung, M. Kim, L. Yin, J. C. Lee, K.-M. Lee, J. A. Rogers, Dissolution chemistry and biocompatibility of silicon-and germanium-based semiconductors for transient electronics. *ACS Appl. Mater. Interfaces* **7**, 9297–9305 (2015).
36. L. S. D. Morley, The thin-walled circular cylinder subjected to concentrated radial loads. *Q. J. Mech. Appl. Math.* **13**, 24 (1960).
37. S. A. Łukasiewicz, Introduction of concentrated loads in plates and shells. *Prog. Aerosp. Sci.* **17**, 109–146 (1976).
38. F. Cavallo, D. S. Grierson, K. T. Turner, M. G. Lagally, "Soft Si": Effective stiffness of supported crystalline nanomembranes. *ACS Nano* **5**, 5400–5407 (2011).
39. D. E. Harris, D. M. Warshaw, Length vs. active force relationship in single isolated smooth muscle cells. *Am. J. Physiol. Cell Physiol.* **260**, C1104–C1112 (1991).
40. M. Bloksgaard, T. M. Leurgans, B. Spronck, M. H. G. Heusinkveld, B. Thorsted, K. Rosenstand, I. Nissen, U. M. Hansen, J. R. Brewer, L. A. Bagatolli, L. M. Rasmussen, A. Irmukhamedov, K. D. Reesink, J. G. R. De Mey, Imaging and modeling of acute pressure-induced changes of collagen and elastin microarchitectures in pig and human resistance arteries. *Am. J. Physiol. Heart Circ. Physiol.* **313**, H164–H178 (2017).
41. M. Szekeres, G. L. Nádasy, G. Dörnyei, A. Szénási, A. Koller, Remodeling of wall mechanics and the myogenic mechanism of rat intramural coronary arterioles in response to a short-term daily exercise program: Role of endothelial factors. *J. Vasc. Res.* **55**, 87–97 (2018).
42. L. Hadjadj, A. Monori-Kiss, E. M. Horváth, A. Heinzlmann, A. Magyar, R. E. Sziva, Z. Miklós, É. Pál, J. Gál, I. Szabó, Z. Benyó, G. L. Nádasy, S. Várbíró, Geometric, elastic and contractile-relaxation changes in coronary arterioles induced by Vitamin D deficiency in normal and hyperandrogenic female rats. *Microvasc. Res.* **122**, 78–84 (2019).
43. N. L. Sehgel, Z. Sun, Z. Hong, W. C. Hunter, M. A. Hill, D. E. Vatner, S. F. Vatner, G. A. Meininger, Augmented vascular smooth muscle cell stiffness and adhesion when hypertension is superimposed on aging. *Hypertension* **65**, 370–377 (2015).
44. S.-K. Kang, S.-W. Hwang, H. Cheng, S. Yu, B. H. Kim, J.-H. Kim, Y. Huang, J. A. Rogers, Dissolution behaviors and applications of silicon oxides and nitrides in transient electronics. *Adv. Funct. Mater.* **24**, 4427–4434 (2014).
45. S.-W. Hwang, H. Tao, D.-H. Kim, H. Cheng, J.-K. Song, E. Rill, M. A. Brenckle, B. Panilaitis, S. M. Won, Y.-S. Kim, Y. M. Song, K. J. Yu, A. Ameen, R. Li, Y. Su, M. Yang, D. L. Kaplan, M. R. Zakin, M. J. Slepian, Y. Huang, F. G. Omenetto, J. A. Rogers, A physically transient form of silicon electronics. *Science* **337**, 1640–1644 (2012).
46. I. Fleming, R. Busse, Molecular mechanisms involved in the regulation of the endothelial nitric oxide synthase. *Am. J. Physiol. Regul. Integr. Comp. Physiol.* **284**, R1–R12 (2003).
47. D. Fulton, J. P. Gratton, T. J. McCabe, J. Fontana, Y. Fujio, K. Walsh, T. F. Franke, A. Papapetropoulos, W. C. Sessa, Regulation of endothelium-derived nitric oxide production by the protein kinase Akt. *Nature* **399**, 597–601 (1999).
48. C.-J. Li, T. H. Elsasser, S. Kahl, AKT/eNOS signaling module functions as a potential feedback loop in the growth hormone signaling pathway. *J. Mol. Signal.* **4**, 1 (2009).
49. V. Gurtu, E. D. Michelakis, A paradigm shift is needed in the field of pulmonary arterial hypertension for its entrance into the precision medicine era. *Circ. Res.* **119**, 1276–1279 (2016).
50. P. Ghataorhe, C. J. Rhodes, L. Harbaum, M. Attard, J. Wharton, M. R. Wilkins, Pulmonary arterial hypertension—Progress in understanding the disease and prioritizing strategies for drug development. *J. Intern. Med.* **282**, 129–141 (2017).
51. L. H. Romer, K. G. Birukov, J. G. Garcia, Focal adhesions: Paradigm for a signaling nexus. *Circ. Res.* **98**, 606–616 (2006).
52. J. S. Choi, Y. Piao, T. S. Seo, Circumferential alignment of vascular smooth muscle cells in a circular microfluidic channel. *Biomaterials* **35**, 63–70 (2014).
53. C. Williams, X. Q. Brown, E. Bartolak-Suki, H. Ma, A. Chilkoti, J. Y. Wong, The use of micropatterning to control smooth muscle myosin heavy chain expression and limit the response to transforming growth factor beta1 in vascular smooth muscle cells. *Biomaterials* **32**, 410–418 (2011).
54. K. Duval, H. Grover, L.-H. Han, Y. Mou, A. F. Pegoraro, J. Fredberg, Z. Chen, Modeling physiological events in 2D vs. 3D cell culture. *Physiology (Bethesda)* **32**, 266–277 (2017).

55. S. Yasotharan, S. Pinto, J. G. Sled, S. S. Bolz, A. Gunther, Artery-on-a-chip platform for automated, multimodal assessment of cerebral blood vessel structure and function. *Lab Chip* **15**, 2660–2669 (2015).
56. J. Xu, C. Chen, X. Jiang, R. Xu, D. Tambe, X. Zhang, L. Liu, B. Lan, K. Cai, L. Deng, Effects of micropatterned curvature on the motility and mechanical properties of airway smooth muscle cells. *Biochem. Biophys. Res. Commun.* **415**, 591–596 (2011).
57. Y. Zhang, X. S. Li, A. G. Guex, S. S. Liu, E. Müller, R. I. Malini, H. J. Zhao, M. Rottmar, K. Maniura-Weber, R. M. Rossi, F. Spano, A compliant and biomimetic three-layered vascular graft for small blood vessels. *Biofabrication* **9**, 025010 (2017).
58. M. F. Fillinger, S. E. O'Connor, R. J. Wagner, J. L. Cronenwett, The effect of endothelial cell coculture on smooth muscle cell proliferation. *J. Vasc. Surg.* **17**, 1058–1067 (1993).
59. G. Di Luozzo, J. Bhargava, R. J. Powell, Vascular smooth muscle cell effect on endothelial cell endothelin-1 production. *J. Vasc. Surg.* **31**, 781–789 (2000).
60. B. Antonny, Mechanisms of membrane curvature sensing. *Annu. Rev. Biochem.* **80**, 101–1023 (2011).

Acknowledgments: Research was performed, in part, at the NIST Center for Nanoscale Science and Technology, Gaithersburg, MD. Confocal imaging was performed at Integrated Imaging Center at Johns Hopkins University and the Microscope Facility at Johns Hopkins School of Medicine, Baltimore, MD. **Funding:** We would like to thank Kley Dom Biomimetics, Windchime, and the Posen Foundation for funding. We also acknowledge support from the NSF (CMMI-1635443 and DMR-1709349). The Zeiss LSM 780 used in this publication was supported by the National Center for Research Resources of the NIH (S10OD016374). **Author contributions:** L.H.R. and D.H.G. conceptualized and supervised the work. Q.J., J.V.P., X.C., and A.H. carried out the device and platform design and fabrication. A.B., J.V.P., Q.J., X.C., and F.B.A. did the experiments. H.W.-F., Q.J., A.B., J.V.P., S.C.K., and L.H.R. accomplished the imaging acquisition and processing. J.L. and T.D.N. performed the theoretical modeling. All authors contributed to data analysis, discussion, and interpretation. Q.J., A.B., J.V.P., D.H.G., and L.H.R. wrote the manuscript with input from all the authors. **Competing interests:** L.H.R., D.H.G., Q.J., J.V.P., A.B., and X.C. have a pending patent (attorney docket number 48317-523001WO) related to the work in this manuscript. L.H.R., D.H.G., Q.J., J.V.P., A.B., and X.C. are inventors on an international patent application related to this work (no. PCT/US2018/056923, filed 22 October 2018). Funding for the study described in this publication was provided by Kley Dom Biomimetics. Under a license agreement between Kley Dom Biomimetics and the Johns Hopkins University, L.H.R., D.H.G., Q.J., J.V.P., A.B., and X.C. and the University are entitled to royalty distributions related to technology described in the study discussed in this publication. This arrangement has been reviewed and approved by the Johns Hopkins University in accordance with its conflict of interest policies. The authors declare no other competing interests. **Data and materials availability:** All data needed to evaluate the conclusions in the paper are present in the paper and/or the Supplementary Materials. Additional data related to this paper may be requested from the authors.

Submitted 25 August 2019
Accepted 3 January 2020
Published 25 March 2020
10.1126/sciadv.aaz2598

Citation: Q. Jin, A. Bhatta, J. V. Pagaduan, X. Chen, H. West-Foyle, J. Liu, A. Hou, D. Berkowitz, S. C. Kuo, F. B. Askin, T. D. Nguyen, D. H. Gracias, L. H. Romer, Biomimetic human small muscular pulmonary arteries. *Sci. Adv.* **6**, eaaz2598 (2020).